

Spin dynamics and magnetic interactions of Mn dopants in the topological insulator Bi_2Te_3 S. Zimmermann,^{1,2} F. Steckel,^{1,3} C. Hess,^{1,3} H. W. Ji,⁴ Y. S. Hor,⁴ R. J. Cava,⁴ B. Büchner,^{1,3} and V. Kataev¹¹*Leibniz Institute for Solid State and Materials Research, IFW Dresden, 01171 Dresden, Germany*²*Institute for Solid State Physics, TU Dresden, 01069 Dresden, Germany*³*Center for Transport and Devices, TU Dresden, 01069 Dresden, Germany*⁴*Department of Chemistry, Princeton University, Princeton, New Jersey 08544, USA*

(Received 3 August 2016; revised manuscript received 2 September 2016; published 21 September 2016)

The magnetic and electronic properties of the magnetically doped topological insulator $\text{Bi}_{2-x}\text{Mn}_x\text{Te}_3$ were studied using electron-spin resonance (ESR) and measurements of static magnetization and electrical transport. The investigated high-quality single crystals of $\text{Bi}_{2-x}\text{Mn}_x\text{Te}_3$ show a ferromagnetic phase transition for $x \geq 0.04$ at $T_C \approx 12$ K. The Hall measurements reveal a p -type finite charge-carrier density. Measurements of the temperature dependence of the ESR signal of Mn dopants for different orientations of the external magnetic field give evidence that the localized Mn moments interact with the mobile charge carriers leading to Ruderman-Kittel-Kasuya-Yosida-type ferromagnetic coupling between the Mn spins of order 2–3 meV. Furthermore, ESR reveals a low-dimensional character of magnetic correlations that persist far above the ferromagnetic ordering temperature.

DOI: 10.1103/PhysRevB.94.125205

I. INTRODUCTION

Topological insulators (TIs) are currently attracting a great deal of interest in the area of condensed-matter research. This interest is due to their unique surface states, which have a linear band dispersion (Dirac cone) and a momentum-locked spin of the charge carriers [1–3]. In such insulating materials, a strong spin-orbit coupling plays a key role. It yields a band inversion in the bulk, whereas the valence and conduction bands ultimately cross at the Dirac point at the material's surface. This gives rise to the gapless conducting surface states that are protected from localization by topology as long as the time-reversal symmetry (TRS) is preserved. However, a magnetic field breaking the TRS can open a gap at the Dirac point. It has been found that this scenario is especially interesting because different phenomena, such as the topological magneto-electric effect [4], the quantized anomalous Hall effect [5,6], the giant magneto-optical effect [7], or magnetic monopoles [8], can occur in TIs.

One way to introduce a magnetic field is to dope a TI with magnetic ions, such as, e.g., Mn, in a concentration sufficient to cause a magnetic order of the dopants and hence an internal magnetic field. In this context, several theoretical works have addressed the magnetic interactions between Mn dopants in the three-dimensional (3D) TIs Bi_2Se_3 , Bi_2Te_3 , and Sb_2Te_3 [9–14]. These materials appear to be advantageous for experiments since they have a relatively large band gap in the bulk and they grow as stoichiometric crystals [2], though residual bulk conductivity due to crystal defects [12] often complicates probing the surface states.

Larson and Lambrecht [9] have studied the entire series of $3d$ transition-metal (TM) dopants in Bi_2Te_3 , Bi_2Se_3 , and Sb_2Te_3 within the local-spin-density approximation (LSDA). Due to the large size mismatch, they predicted no hybridization of the $3d$ orbitals for the early TM ions. Beyond half-filling of the $3d$ shell, stronger hybridized covalent bonded states were expected. In a later work, Niu *et al.* [10] found by first-principles calculations that the $3d$ orbitals of the Mn^{3+} dopants ($3d^4$) in Bi_2Te_3 show a strong hybridization with the $5p$ orbitals of the surrounding Te ions. In combination with the octahedral coordination, this produces a strong crystal-

field splitting resulting in a high spin $t_{2g}^3 e_g^1$ configuration. The coupling of the Mn impurities was explained by a superexchange mechanism via the Te ions. In contrast, Zhang *et al.* [12] predicted a valence state of $2+$ for Mn in Bi_2Te_3 , in agreement with experimental findings [15–17]. This was supported by a recent work by Li *et al.* [13] in which strong indications for a half-filled $3d^5$ configuration (Mn^{2+}) with an atomlike high spin state (Hund's rules) were found. Again, due to the large size mismatch, the $3d$ orbitals do not hybridize with the Te $5p$ orbitals and thus no dominant crystal-field splitting is predicted. The ferromagnetic coupling of the Mn dopants is explained by the weak but long-range Ruderman-Kittel-Kasuya-Yosida (RKKY) interaction. Also recently Vergniory *et al.* [14] investigated the series of $3d$ TM dopants in Bi_2Te_3 , Bi_2Se_3 , and Sb_2Te_3 by first-principles calculations. Strong hybridization of the $3d$ orbitals with the host is taken into account, and the exchange integrals J between the different neighbors are calculated. In their findings, the coupling J between the atomic layers is of the double exchange type, and within a layer the exchange is mediated by free carriers. For thin films where the bulk conductivity is reduced or extinguished, other mechanisms were proposed. Thus, it has been predicted that the magnetic coupling is mediated by the surface states [18] or by an enhanced Van Vleck mechanism [5].

Electron-spin resonance (ESR) spectroscopy is a valuable tool to probe the spin dynamics and interactions of localized moments dissolved in a nonmagnetic conducting matrix [19]. With this aim, ESR studies were previously reported for Bi_2Te_3 [20,21] and Bi_2Se_3 [22] doped with Gd. Von Bardeleben *et al.* [23] investigated Mn-doped thin films of Bi_2Se_3 in the ferromagnetic regime ($T \leq 6$ K) by means of ferromagnetic resonance. Another paper [24] reported ESR studies on $\text{Bi}_{2-x}\text{Mn}_x\text{Te}_3$ nanocrystals that are embedded in a glass matrix.

In the present work, to obtain experimental insights into the mechanism of magnetic interactions of TM dopants in a 3D topological insulator, we have systematically investigated with ESR spectroscopy a series of high-quality single crystals of $\text{Bi}_{2-x}\text{Mn}_x\text{Te}_3$ with doping concentrations $x = 0.01, 0.02,$

0.04, 0.07, and 0.09. The ESR study was complemented by measurements of magnetization and electrical transport. A combined analysis of the experimental data enables us to conclude that the coupling between the Mn spins that gives rise to ferromagnetic order in $\text{Bi}_{2-x}\text{Mn}_x\text{Te}_3$ with $x \geq 0.04$ at $T_C \approx 9\text{--}12$ K occurs via the RKKY mechanism involving as mediators the mobile charge carriers. Interestingly, ESR measurements reveal that short-range ferromagnetic correlations are still present at temperatures substantially larger than T_C , suggestive of a predominantly two-dimensional character of magnetic exchange associated with the layered structure of $\text{Bi}_{2-x}\text{Mn}_x\text{Te}_3$.

The paper is organized as follows. In Sec. II, sample particulars and information on experimental methods are given. Experimental magnetization, electrical transport, and ESR data are described and analyzed in Sec. III. A common discussion of the results obtained is presented in Sec. IV, followed by the main conclusions in Sec. V.

II. EXPERIMENTAL DETAILS

A. Samples

The tetradymite crystal structure (space group $R\bar{3}m$) of Bi_2Te_3 has a rhombohedral lattice where five atomic planes form quintuple layers Te-Bi-Te-Bi-Te stacked along the c axis. Within the quintuple layers, the bonding is much stronger than the van der Waals-type connection in between the layers. Thus the crystals naturally cleave parallel to the ab basal plane. The coordination of Bi^{3+} by Te^{2-} ions is roughly octahedral with a small trigonal distortion.

The series of high-quality single crystals of $\text{Bi}_{2-x}\text{Mn}_x\text{Te}_3$ with doping concentrations of $x = 0.01, 0.02, 0.04, 0.07,$ and 0.09 investigated in this work was grown by a modified Bridgman process from high-purity elemental Bi (99.999%), Mn (99.99%), and Te (99.999%), as explained in detail by Hor *et al.* [15]. They were thoroughly characterized by different physical methods in Ref. [15]. In particular, it was shown that the Mn dopants occupy the Bi sites and that they are homogeneously distributed and not clustered, i.e., the grown single crystals are true dilute magnetic semiconductors. For doping levels of $x \geq 0.04$, a transition to a ferromagnetic state with $T_C \approx 9\text{--}12$ K and an easy axis parallel to the c axis was observed. The electronic transport measurements revealed p -type charge carriers. Furthermore, samples from the same batch have been investigated with x-ray-absorption spectroscopy (XAS) and photoemission spectroscopy (PES) [16,17]. It was shown that Mn possesses a $3d^5$ configuration as a ground state. The $3d^5$ configuration corresponds to a Mn^{2+} valence state and is consistent with the known acceptor behavior when substituting Bi^{3+} [15].

B. Experimental methods

The measurements of the magnetization were performed with a superconducting quantum interference device from Quantum Design equipped with a vibrating sample magnetometer (VSM-SQUID). The available magnetic fields amount to 7 T and the temperature can be set between 1.8 and 300 K. The external magnetic field was always applied perpendicular to the crystallographic c axis of the studied sample.

For the electrical transport studies, the samples were mounted in a homemade probe head and contacted with silver paste in a standard four- or six-point configuration. The current was always applied in the basal ab plane in the x direction, and the voltage was measured either in the same direction or in the perpendicular y direction to obtain the resistivities ρ_{xx} and ρ_{xy} , respectively. The probe head was inserted in a magnetocryostat from Oxford Instruments with a maximal field of 15 T and the available temperature range 4.2–300 K. The external magnetic field was applied parallel to the crystallographic c axis of the sample, which is denoted as the z axis.

ESR was measured with a commercial X-band spectrometer from Bruker with a rectangular resonator working in the TE_{103} mode at the microwave frequency $\nu \simeq 9.57$ GHz. The magnetic field could be swept from 0 to 0.9 T. The signals were detected with the lock-in technique, for which the external field was modulated by a small ac field with an amplitude of 0.8 mT at a frequency of 100 kHz. As a result, the measured ESR signal is the field derivative of the absorbed microwave power $dP(H)/dH$. The samples were placed in a helium gas-flow cryostat from Oxford Instruments that enabled temperature-dependent measurements between 3.7 and 300 K. The cryostat was equipped with a goniometer for rotating the sample with respect to the external magnetic field. To increase the ESR signal intensity, several cleaved pieces of the crystal were measured simultaneously by placing them on a substrate with the crystallographic c axis perpendicular to the substrate plane. The alignment of the a and b axes was not attempted since only minor anisotropy effects within the ab plane are expected.

III. EXPERIMENTAL RESULTS AND ANALYSIS

A. Magnetization

The temperature dependence of the magnetization $M(T)$ measured for various doping concentrations ($x = 0.01, 0.04, 0.07,$ and 0.09) is shown in Fig. 1(a). During the measurements, a weak external magnetic field of $\mu_0 H = 0.1$ T was applied perpendicular to the c axis. This field is in the range where M depends linearly on H . For doping concentrations $x \geq 0.04$, a transition to the ferromagnetic regime at $T \approx 12$ K is visible as a kink in the $M(T)$ curve. A precise determination of the transition temperature T_C has already been done by Hor *et al.* [15] using Arrott plots. The respective values are summarized in Table I. In Fig. 1(b), the inverse magnetic susceptibility $1/\chi = H/M$ as well as the fit functions following the Curie-Weiss law $\chi - \chi_0 = C/(T - \theta_{CW})$ for $T > T_C$ are plotted. Here, χ_0 accounts for a sum of the temperature-independent diamagnetic, Van Vleck, and Pauli susceptibilities. The linear dependence demonstrates the paramagnetic behavior in a broad temperature range, and the extracted values for the Curie-Weiss temperature θ_{CW} are again in good agreement with Ref. [15]. From the Curie constant $C = x N_A \mu_{\text{eff}}^2 / 3k_B$, the effective magnetic moment μ_{eff} per Mn ion can be calculated. Here, N_A and k_B are the Avogadro number and the Boltzmann constant. The obtained values lie in between $5.5\mu_B$ and $5.8\mu_B$, which is only slightly below the expected value for the Mn^{2+} ion calculated from $\mu_{\text{cal}} = g\sqrt{S(S+1)} = 5.9\mu_B$ with the spin $S = \frac{5}{2}$ and the g factor $g \approx 2$ (see Sec. III C). Only for

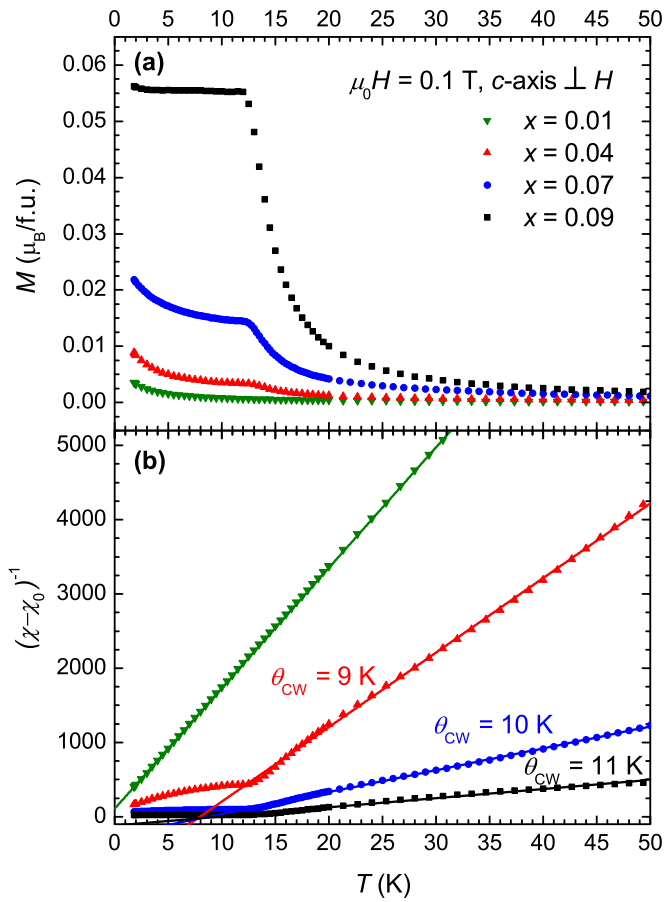


FIG. 1. Temperature dependence of (a) the static magnetization $M(T)$ and (b) the inverse magnetic susceptibility $\chi(T)^{-1}$ of $\text{Bi}_{2-x}\text{Mn}_x\text{Te}_3$, measured in a weak external field H for various doping concentrations x . The external magnetic field $\mu_0 H = 0.1$ T was applied perpendicular to the crystallographic c axis. The solid lines correspond to Curie-Weiss fit functions of the linear high-temperature regime $(\chi - \chi_0)^{-1} = (T - \theta_{\text{CW}})/C$ (see Sec. III A).

$x = 0.04$ is the value $\mu_{\text{eff}} = 4.3\mu_B$ somewhat lower, which may be a hint of a lower actual value of x . Altogether the estimates of μ_{eff} point to a Mn^{2+} valence state in agreement with the XAS results in Ref. [16]. The 2+ valency of Mn is further proved by the ESR data (see Sec. III C).

B. Electrical transport

To obtain insights into the electronic properties, the temperature dependence of the resistivity $\rho_{xx}(T)$ was measured.

TABLE I. Magnetic properties of $\text{Bi}_{2-x}\text{Mn}_x\text{Te}_3$ single crystals. Values measured by Hor *et al.* [15] are added for comparison.

x	T_C [15] (K)	θ_{CW} [15] (K)	θ_{CW} (K)	μ_{eff} (μ_B)	$\mu_0 \frac{d\Delta H}{dT}$ (T/K)
0.01		-0.7	-0.7	5.5	
0.04	9	11	9	4.3	1.21
0.07			10	5.5	1.19
0.09	12	13	11	5.8	0.89

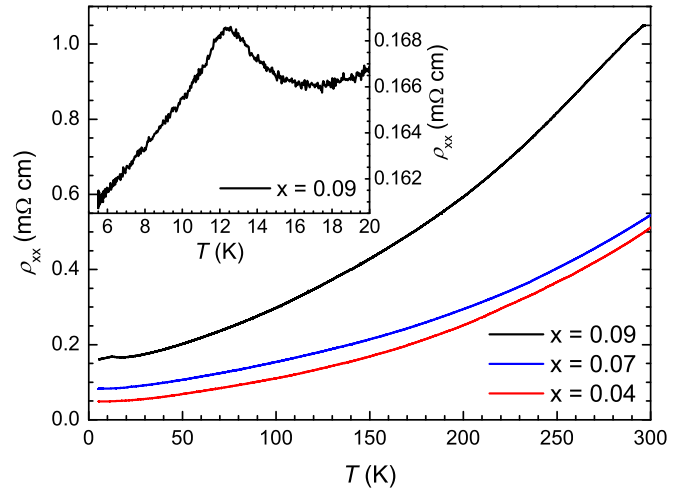


FIG. 2. Temperature dependence of the resistivity parallel to the charge current $\rho_{xx}(T)$ of $\text{Bi}_{2-x}\text{Mn}_x\text{Te}_3$ for various doping concentrations x . The inset shows the enlarged low-temperature regime for $x = 0.09$.

Furthermore, Hall resistivity $\rho_{xy}(T, H)$ measurements were performed to determine the charge-carrier density of the samples to be investigated by ESR. The resistivity (Fig. 2) shows a metallic temperature dependence as expected for a heavily doped semiconductor. Consistent with previous measurements on crystals from the same batch [15], the resistivity increases with doping concentration. This could be explained by an increased number of scattering centers with higher Mn doping. As can be seen in the inset of Fig. 2, the resistivity of the highest doped sample shows an anomaly around 12 K associated with the ferromagnetic phase transition. In this case, the increased scattering is connected with an enhancement of magnetic fluctuations near the phase transition, and it was similarly observed before in comparable systems [25].

The Hall measurements are antisymmetrized with respect to the sign of the magnetic field ($\rho_{xy} = \frac{1}{2}[\rho_{xy}^{H>0} - \rho_{xy}^{H<0}]$) to exclude the influence of the contact geometry. As exemplarily shown in Fig. 3 for $x = 0.07$, the Hall resistivity shows a linear field dependence $\rho_{xy} = R_H \mu_0 H$ at $T = 300$ K. With the Hall constant R_H , the charge-carrier density $p_{\text{Hall}} = \frac{1}{eR_H}$ is calculated from the high-field ($\mu_0 H \geq 11$ T) values of ρ_{xy} because in this range the magnetization is saturated [15]. As can be seen in Fig. 4, the values of p_{Hall} for all three samples are positive and in the range $10^{19} \lesssim p_{\text{Hall}} \lesssim 10^{20} \text{ cm}^{-3}$. p_{Hall} increases with x , thus confirming the acceptor behavior of Mn^{2+} dopants. The charge-carrier concentration is lower than the doping concentration [$c_{\text{Mn}} \approx (2-5) \times 10^{20} \text{ cm}^{-3}$], showing that the crystals are partially electrically compensated.

With decreasing temperature the field dependence of ρ_{xy} becomes nonlinear, especially for low fields (Fig. 3). A similar behavior was observed in Bi_2Te_3 by Rischau *et al.* [26] giving two possible explanations: the anisotropy of the Fermi surface and the occupation of a second valence band. The anisotropy of the Fermi surface was described with a six-ellipsoidal model by Köhler [27], where it was also stated that for $p > 4 \times 10^{-18} \text{ cm}^{-3}$ a second valence band is occupied. A

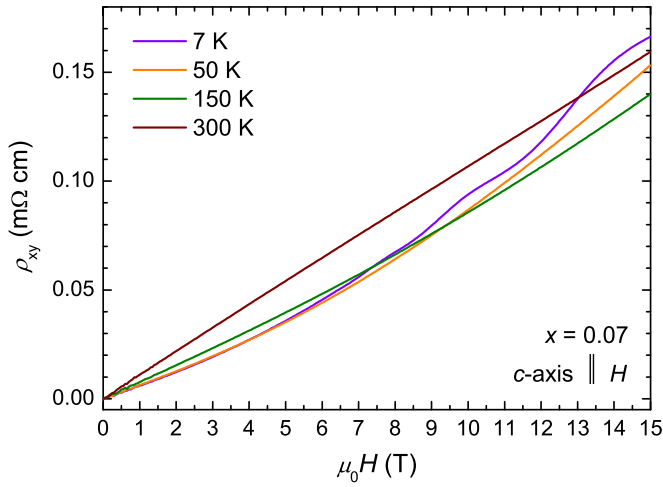


FIG. 3. Magnetic-field dependence of the Hall resistivity $\rho_{xy}(H)$ of $\text{Bi}_{2-x}\text{Mn}_x\text{Te}_3$ for $x = 0.07$ at various temperatures. Measurements were performed in the ab basal plane; the external field H was applied normal to this plane ($\parallel c$ axis).

further signature of a second valence band is the temperature dependence of p_{Hall} [28,29]. It becomes more pronounced with increasing x , which is equivalent to a stronger shift of the Fermi level.

In addition to the nonlinearity at low fields, Shubnikov–de Haas (SdH) oscillations are visible for $x = 0.07$ at high fields at a low temperature $T = 7$ K (Fig. 3). The frequency of the oscillation F is proportional to the cross section of the Fermi surface S_c perpendicular to the external field H ($H \parallel c$):

$$\frac{1}{F} = \Delta \left(\frac{1}{B} \right) = \frac{2\pi e}{\hbar S_c}. \quad (1)$$

F can be easily determined from the period of the oscillations Δ when plotting the derivative of ρ over B^{-1} (not shown). Following the six-ellipsoidal model [27,30], an anisotropy

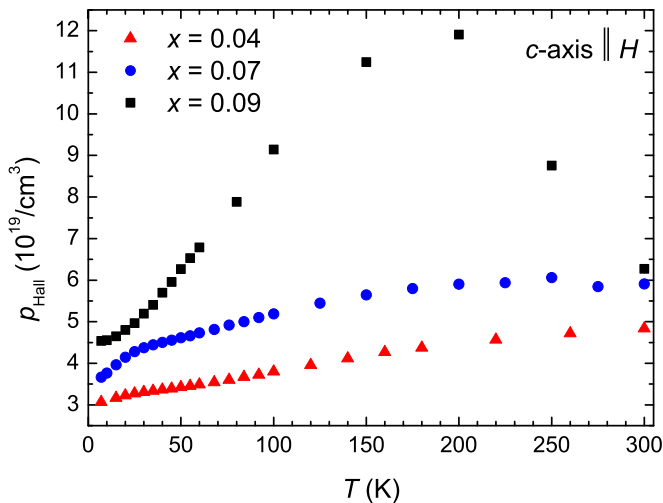


FIG. 4. Temperature dependence of the charge-carrier density $p_{\text{Hall}}(T)$ of $\text{Bi}_{2-x}\text{Mn}_x\text{Te}_3$ for various x . The values were obtained from the Hall resistivity in the high-field region $\mu_0 H \geq 11$ T (see the text).

factor $\eta = 1.515$ can be introduced to calculate the volume of the ellipsoid V from S_c . Taking also into account a factor of 6 for the degeneracy of the levels, the charge-carrier density can be estimated as

$$p_{\text{SdH}} = 6 \frac{2V}{(2\pi)^3} \approx 6 \frac{2}{(2\pi)^3} \frac{4}{3\sqrt{\pi}} \eta S_c^{\frac{3}{2}}. \quad (2)$$

The observed frequency $F = 34.6$ T yields $p_{\text{SdH}} = 1.1 \times 10^{19}$ cm^{-3} . This is in the same order of magnitude but somewhat smaller than the value extracted from the Hall resistivity $p_{\text{H}} = 3.7 \times 10^{19}$ cm^{-3} . Similar differences have been observed for Bi_2Te_3 [27,28,31] and Sb_2Te_3 [29] and prove the contribution of a second valence band to p_{Hall} . A second SdH frequency was not observed, probably due to a smaller effective mass that enters the amplitude of the oscillation.

C. Electron-spin resonance

ESR measurements at the X-band frequency $\nu \simeq 9.57$ GHz were performed for five single crystals of $\text{Bi}_{2-x}\text{Mn}_x\text{Te}_3$ with different doping concentrations $x = 0.01, 0.02, 0.04, 0.07$, and 0.09 . A single resonance line with a pronounced angular and temperature dependence was observed. The intensity of the signal increases with x , so that the resonance signal can be undoubtedly assigned to the Mn dopants. The g factor has a value $g \approx 2$ (for $T \geq 50$ K) very close to the free-electron value $g = 2.0023$. Such a g value is very typical for ESR of the Mn^{2+} ions with $S = \frac{5}{2}$ and $L = 0$ [32], thus confirming the 2+ valency of the Mn dopants. For $x \leq 0.02$, the intensity is weak so that the signal can only be observed in a narrow temperature range and for the orientation of the magnetic field close to the ab basal plane. Therefore, systematic studies are presented for the samples with $x \geq 0.04$ with a particular focus on the sample with the highest doping ($x = 0.09$).

A series of typical spectra [absorption derivatives $dP(H)/dH$] for different temperatures is plotted in Fig. 5. The ESR signal of all studied samples is always a single line. Its shape is asymmetric with a ratio of the positive and negative

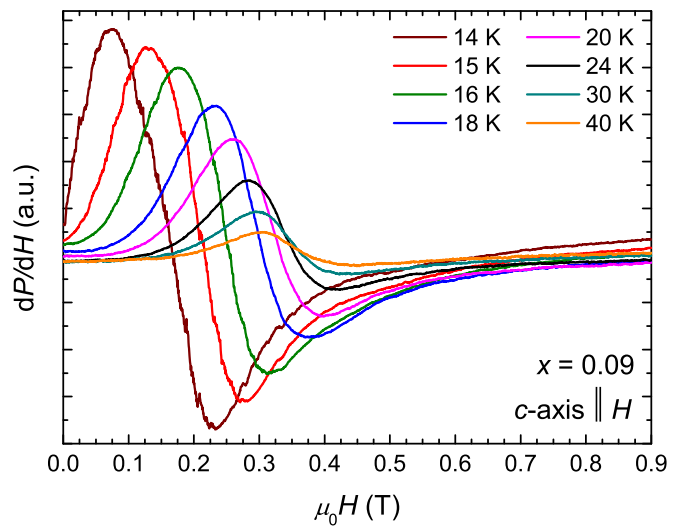


FIG. 5. ESR spectra of the $\text{Bi}_{2-x}\text{Mn}_x\text{Te}_3$ sample with the highest doping level $x = 0.09$ for various temperatures. The external magnetic field H was applied parallel to the crystallographic c axis.

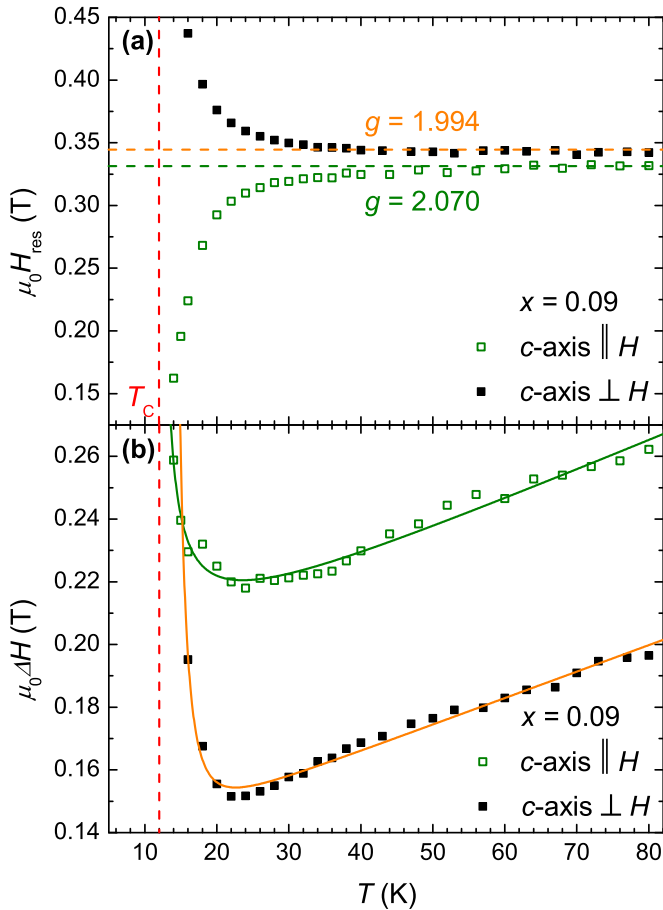


FIG. 6. Temperature dependence of the resonance field $H_{\text{res}}(T)$ (a) and the linewidth $\Delta H(T)$ (b) of $\text{Bi}_{2-x}\text{Mn}_x\text{Te}_3$ with $x = 0.09$. The external magnetic field H is applied parallel and perpendicular to the crystallographic c axis. The vertical dashed line marks the transition temperature T_C . The horizontal dashed lines in (a) denote the averaged values of the resonance field in the range $T = 50$ – 80 K with the corresponding values of g . The solid lines in (b) are fits according to Eq. (4).

peaks of the absorption derivative equal to 2.5. The signals can be fitted well with a Dysonian line profile, which is a mixture of the Lorentzian absorption and dispersion derivatives yielding an accurate determination of the resonance field and linewidth (Fig. 6). A Dysonian ESR line shape is typically observed for localized magnetic moments in a metallic host, and it is due to a finite penetration depth of the microwaves in a bulk metallic sample [19]. Similar line shapes were also observed in Gd-doped single crystals of Bi_2Te_3 [20,21] and Bi_2Se_3 [22]. Remarkably, no fine or hyperfine structure of the spectrum typical for ESR of isolated Mn^{2+} ions [32] is observed. A collapse of the spectrum into a single line with the Lorentzian (Dysonian) shape gives evidence for magnetic exchange interaction between the Mn spins that averages and narrows the fine and the hyperfine structure and also reduces inhomogeneous line broadening originated from the dipole-dipole interactions (exchange narrowing effect [19,33,34]).

As can be seen in Fig. 6(a), the resonance field H_{res} is practically constant at high temperatures. The dotted lines in Fig. 6(a) represent the average for both orientations of the

magnetic field in the range $T = 50$ – 80 K, and they correspond to g factors of $g = 1.994$ for $H \parallel c$ and $g = 2.070$ for $H \perp c$. A slight anisotropy of the g factor arises due to a small admixture of the high-energy multiplet with nonzero orbital momentum to the ground-state spin-only multiplet of Mn^{2+} [32]. In addition, in conducting systems a covalent bonding between localized moments and conducting bands can lead to a shift of the g factor [19]. The degree of covalent bonding could depend on the orientation of the magnetic orbitals resulting in an anisotropy of g . For the samples with $x = 0.04$ and 0.07 , nearly identical values for H_{res} with the same temperature dependence were observed (not shown).

Below $T \approx 40$ K, the resonance field develops a remarkable temperature dependence for both field orientations [Fig. 6(a)]. For the $H \parallel c$ axis, H_{res} shifts to lower fields while it increases for the perpendicular orientation. The shifts increase rapidly when approaching the transition temperature T_C . In a ferromagnet, the shift of the magnetic resonance signal from its paramagnetic position $H_{\text{res}}^{\text{param}} = (h/g\mu_B)\nu$ determined by the g factor is due to the shape anisotropy as well as the magnetocrystalline anisotropy of the easy-axis or easy-plane type [35]. Magnetization measurements below T_C by Hor *et al.* [15] have revealed that $\text{Bi}_{2-x}\text{Mn}_x\text{Te}_3$ is an easy-axis ferromagnet with the magnetic easy axis parallel to the crystallographic c axis. From the $M(H)$ curves, the saturation magnetization $\mu_0 M_s \approx 0.01$ T and the anisotropy field $\mu_0 H_A \approx 1$ T were also determined [15]. In this case, the ferromagnetic resonance signal should shift with respect to $H_{\text{res}}^{\text{param}}$ to smaller fields for $H \parallel c$ and to higher fields for $H \perp c$ [35]. On the other hand, the shape anisotropy of the platelike single crystalline sample would cause an opposite effect [36]. Comparing the magnetocrystalline anisotropy constant $K_u = (\mu_0/2)H_A M_s \approx 4$ kJ/m³ with the shape anisotropy constant K_d , it becomes clear that even for the limiting case of a thin layer [$K_d = -(\mu_0/2)(4\pi/3)M_s^2 \approx -0.2$ kJ/m³], the intrinsic magnetocrystalline part of the anisotropy is dominating. In the present work, no signals could be detected below T_C because ferromagnetic resonance is out of the frequency range of the used X-band spectrometer ($\nu = 9.6$ GHz) [37] due to the opening of the magnetic anisotropy gap for the ESR excitation, $\nu_{\text{MA}} = (g\mu_0\mu_B/h)H_A \approx 28$ GHz. However, the dependence of the shifts of the ESR signal on the field orientation in the paramagnetic state above T_C strongly resembles the shifts expected in the ferromagnetically ordered state with the dominant easy-axis type ($\parallel c$ axis) magnetocrystalline anisotropy. Thus, it is reasonable to conclude that these shifts originate from the short-range ferromagnetic correlations between the Mn spins, which could be static on the fast time scale of an ESR measurement of the order $\nu^{-1} \sim 100$ ps. Considering the temperature dependence of H_{res} , these correlations persist up to temperatures much higher than T_C , which is a typical signature of low-dimensional magnets [38]. Indeed, a low-dimensional character of the spin-spin interactions can be expected in the two-dimensional crystallographic structure of $\text{Bi}_{2-x}\text{Mn}_x\text{Te}_3$. This observation is supported by the theoretical findings of Vergniory *et al.* [14], where the exchange interaction in the atomic layers was found to be stronger than that in between the layers. The temperature dependence of the Mn^{2+} ESR linewidth also reveals two distinct regimes as depicted in Fig. 6(b) for two orientations of the external field. For

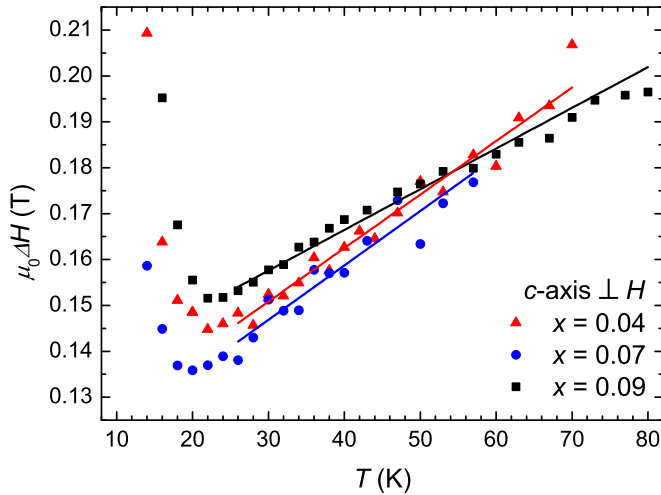


FIG. 7. Temperature dependence of the linewidth $\Delta H(T)$ of $\text{Bi}_{2-x}\text{Mn}_x\text{Te}_3$ for various doping concentrations x . The external magnetic field H was applied perpendicular to the crystallographic c axis. The solid lines are linear fits for $T \geq 25$ K.

$T \gtrsim 25$ K, the linewidth increases linearly with T , which is an expected type of dependence for ESR of paramagnetic local moments in a metal. It has been described by Korringa [19,39] as a result of the relaxation of localized spins due to their coupling to the spins of conduction electrons with energies within the $k_B T$ region around the Fermi energy E_F . Thus, the so-called Korringa relaxation rate scales linearly with temperature. The temperature-dependent part of the linewidth due to the Korringa relaxation reads [19,39]

$$\Delta H_{\text{Kor}}(T) = \frac{2H_{\text{res}}}{\hbar\nu} [D(E_F)J_{\text{cd}}]^2 k_B T. \quad (3)$$

Here $D(E_F)$ is the density of states at the Fermi level and J_{cd} is the exchange integral between the conduction electrons (or holes) and the d electrons of the Mn impurities. The observation of the linear Korringa dependence is proof of the coupling between localized d electrons with the conducting holes.

The temperature dependence of ΔH for three investigated samples with x equal to 0.04, 0.07, and 0.09 is compared in Fig. 7. The linear fit in the temperature range above 25 K yields the values of the slope $b = \mu_0(d\Delta H/dT)$ equal to (1.21 ± 0.17) , (1.19 ± 0.12) , and (0.89 ± 0.10) mT/K for $x = 0.04, 0.07,$ and 0.09 , respectively. The Korringa slope b changes only slightly with the doping concentration x . Hence, the system shows a non-bottlenecked behavior, i.e., the coupled subsystems of the Mn localized spins, conducting holes, and the lattice are in equilibrium, and the spin angular momentum of Mn transferred to the reservoir of charge carriers has enough time to decay to the lattice [19]. For $T \lesssim 25$ K, the linewidth increases rapidly when approaching the transition temperature T_C . This critical broadening can be ascribed to the slowing down of the spin fluctuations resulting from the enhancement of magnetic correlations in the short-range spin-correlated regime above T_C . Taking into account a temperature-independent term ΔH_0 and the linear-in- T Korringa term [Eq. (3)], the $\Delta H(T)$ dependence

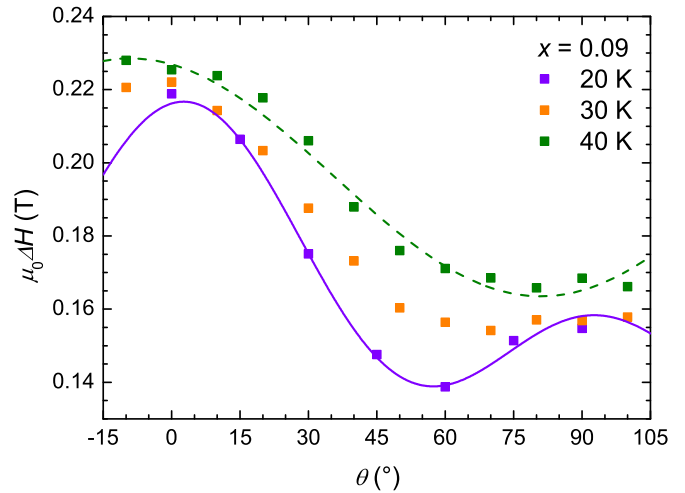


FIG. 8. Angular dependence of the linewidth $\Delta H(\theta)$ of $\text{Bi}_{2-x}\text{Mn}_x\text{Te}_3$ for $x = 0.09$. θ is the angle between the external magnetic field H and the crystallographic c axis. The lines correspond to fits of the data (see the text).

in the entire temperature range can be described as

$$\Delta H(T) = \Delta H_0 + \Delta H_{\text{Kor}}(T) + c \left(\frac{|T - T_C|}{T_C} \right)^{-\beta}. \quad (4)$$

Here, the last term represents the broadening near T_C with the critical exponent β and the temperature-independent prefactor c . As can be seen in Fig. 6(b), the experimental data are described well by Eq. (4). The determination of β is quite sensitive to the value of T_C resulting in an appreciable uncertainty. With $T_C = 12$ K, the critical exponent $\beta \approx 0.9 \pm 0.3$ is obtained for $H \parallel c$. This is close to the theoretically expected value for a three-dimensional Heisenberg magnet $\beta_{\text{Heisenberg}}^{3D} = 1$ [38]. Following the arguments of Benner and Boucher [38] in the critical regime, the moments can behave Ising-like due to the internal fields. Comparing the determined exponent with the Ising critical exponents, one can see that it lies in between the three- and two-dimensional values $\beta_{\text{Ising}}^{3D} = 0.6$ and $\beta_{\text{Ising}}^{2D} = 1.3$, respectively, in accord with the presumed low-dimensional character of the Mn-Mn magnetic correlations in $\text{Bi}_{2-x}\text{Mn}_x\text{Te}_3$. For $H \perp c$, a steeper slope is observed with $\beta \approx 2.8 \pm 0.6$ since here the field is oriented perpendicular to the easy axis. For $x = 0.04$ and 0.07 , similar values for the critical exponent were determined. Finally, the angular dependence of the linewidth is shown in Fig. 8 for three different temperatures. For $T = 20$ K, it follows that $\Delta H \propto (3 \cos^2 \theta - 1)^2$, which has a characteristic minimum at the so-called “magic” angle 55° (solid line), a dependency that results from the anisotropic dipole-dipole interaction. This observation is characteristic for two-dimensional systems in the critical regime [38] where the slowing down of the spin dynamics makes the exchange narrowing of the ESR signal less effective and enhances the dipole-dipole contribution to the linewidth. For higher temperatures, this effect is less dominant. For $T = 40$ K, the angular dependence resembles $\Delta H \propto (\cos^2 \theta + 1)$ as marked by the dashed line. This behavior was also observed in $\text{Bi}_{2-x}\text{Mn}_x\text{Se}_3$ [23]. It is characteristic for three-dimensional systems with dominant

exchange narrowing, and it signifies the occurrence of the uncorrelated truly paramagnetic regime in $\text{Bi}_{2-x}\text{Mn}_x\text{Te}_3$ above $T \approx 40$ K. The $\Delta H(\theta)$ dependence at $T = 30$ K appears to be intermediate between these two types.

IV. ELECTRONIC PROPERTIES AND EXCHANGE INTEGRALS

As follows from Eq. (3), the Korringa slope $b = \mu_0 d\Delta H/dT$ depends on the density of states at the Fermi level, $D(E_F)$, and the exchange integral between conducting holes and localized Mn moments, J_{cd} . It is possible to estimate J_{cd} by calculating $D(E_F)$ from the charge-carrier density p_{Hall} with $D(E_F) = 4\frac{m^*}{\hbar^2}(3\pi^2 p_{\text{Hall}})^{1/3}$ using the simple model of a three-dimensional electron gas. From our transport measurements in Sec. III B, the mobile charge carriers in $\text{Bi}_{2-x}\text{Mn}_x\text{Te}_3$ are holes with a charge-carrier density in the range $10^{19} \text{ cm}^{-3} \lesssim p_{\text{Hall}} \lesssim 10^{20} \text{ cm}^{-3}$. The effective mass of the valence band $m^* = 0.35m_e$ was determined by Köhler [27]. The values of the slope b are similar for the three samples ($x = 0.04, 0.07, \text{ and } 0.09$), resulting in similar values for the exchange constant in the range $J_{cd} \approx 0.5\text{--}0.7$ eV. This is a typical scale for magnetically doped semiconductors ($J_{cd} \lesssim 1$ eV) [40]. For V-doped Sb_2Te_3 , a larger value was observed with $J_{cd} = 5.3$ eV. Li *et al.* [13] had predicted $J_{pd} = 1.4$ eV for the exchange between the Mn d orbitals and the Te p orbitals that form the valence band. The above estimation is oversimplified since it ignores the anisotropy of the Fermi surface (see Ref. [27]) and the probable existence of a second partially occupied valence band, as is suggested by the analysis of our transport measurements. In a two-band model, the Korringa relaxation rate should have two contributions, making it difficult to calculate J_{cd} without further input. Nevertheless, the simple one-band model can be used to clarify the consistency of our data. For the RKKY interaction, the exchange integral J_{ij} between two localized moments at sites i and j is defined as

$$J_{ij} = \frac{3m^*V^2}{4\pi\hbar^2} J_{cd}^2 \frac{\sin(2k_F r) - 2k_F r \cos(2k_F r)}{r^4}. \quad (5)$$

Here, V is the volume of the unit cell, k_F is the Fermi vector, and r is the distance between the moments at sites i and j that can be calculated from the Mn concentration. Using again the model of the 3D electron gas and the estimated values for J_{cd} , one obtains $|J_{ij}| \approx 2\text{--}3$ meV with $J_{ij} < 0$ (ferromagnetic). This agrees with theoretical predictions for Mn in Bi_2Te_3 from Vergniory *et al.* [14] ($|J_{ij}| \lesssim 2$ meV) and Henk *et al.* [11] ($|J_{ij}| \approx 2\text{--}3$ meV). In addition, the Curie-Weiss temperature can be calculated [40] with $\theta_{\text{CW}} = [2S(S+1)/3k_B](xz|J_{ij}|/5)$ using J_{ij} from above, $S = 5/2$, and the number of nearest neighbors $z = 6$. The results are values in the range $\theta_{\text{CW}} \approx 3\text{--}9$ K that increase with the doping concentration x . Considering the crudeness of the approximation, these values are in fair agreement with the measured values $\theta_{\text{CW}} \approx 9\text{--}11$ K (Table I).

Therefore, the exchange coupling is presumably dominated by one band instead of two. This would imply different values of $D(E_F)$, J_{cd} , or m^* for the proposed two bands.

Furthermore, the coupling of the Mn moments and the mobile holes results in an anisotropy of H_{res} in the paramagnetic regime at $T \geq 40$ K (Fig. 6). The additional contribution to the anisotropy due to the crystal-field effect originates from the anisotropy of the band structure [19], which in this case is most likely determined by the layered crystal structure.

V. CONCLUSION

The spin dynamics and magnetic interactions between Mn dopants in $\text{Bi}_{2-x}\text{Mn}_x\text{Te}_3$ high-quality single crystals have been investigated using electron-spin-resonance spectroscopy and complementary measurements of the static magnetization and transport properties. Magnetization measurements show the existence of a ferromagnetic phase below a transition temperature $T_C \approx 12$ K for $x \geq 0.04$. The electrical transport measurements reveal p -type conductivity with a charge-carrier density in the range $10^{19} \text{ cm}^{-3} \lesssim p_{\text{Hall}} \lesssim 10^{20} \text{ cm}^{-3}$. A detailed study of the temperature and orientational dependences of the ESR signal of the Mn^{2+} dopants reveals two distinct regimes: (i) a paramagnetic uncorrelated regime above $T \sim 20\text{--}40$ K, which is characterized by the relaxation of Mn spins on the mobile charge carriers (Korringa relaxation); and (ii) a critical spin-correlated regime below $T \sim 20\text{--}40$ K, which is characterized by anisotropic shifts of the position of the Mn^{2+} ESR signal and its critical broadening by approaching the ordering temperature T_C . The observed Korringa behavior of the ESR linewidth gives evidence that the localized Mn moments are exchange-coupled to the mobile holes. A combined qualitative discussion of the ESR and transport data enables the conclusion that the charge carriers mediate ferromagnetic interaction between the Mn dopants via the RKKY mechanism with a coupling strength $|J_{ij}| \approx 2\text{--}3$ meV, thus confirming the theories of Li *et al.* [13] and Vergniory *et al.* [14], where RKKY-type interactions are predicted. The critical behavior of the ESR signal at lower temperatures indicates a gradual development of the Mn spin-spin correlations with the easy-axis type ($\parallel c$ axis) magnetic anisotropy. These correlations are visible in the ESR data at temperatures far above T_C , suggesting a low-dimensional character for the magnetic exchange between the Mn dopants that can be ascribed to the layered crystal structure. Our experimental findings appear useful for a deeper understanding of magnetic interactions in magnetically doped topological insulators.

ACKNOWLEDGMENTS

This work was supported in part by the Deutsche Forschungsgemeinschaft (DFG) through project KA 1694/8-1, through the Collaborative Research Center SFB 1143, and at Princeton by the NSF MRSEC program, Grant No. DMR-1420541.

[1] M. Z. Hasan and C. L. Kane, *Rev. Mod. Phys.* **82**, 3045 (2010).
 [2] M. Z. Hasan and J. E. Moore, *Annu. Rev. Condens. Matter Phys.* **2**, 55 (2011).

[3] X.-L. Qi and S.-C. Zhang, *Rev. Mod. Phys.* **83**, 1057 (2011).
 [4] X. L. Qi, T. L. Hughes, and S. C. Zhang, *Phys. Rev. B* **78**, 195424 (2008).

- [5] R. Yu, W. Zhang, H. J. Zhang, S. C. Zhang, X. Dai, and Z. Fang, *Science* **329**, 61 (2010).
- [6] C. Z. Chang, J. S. Zhang, X. Feng, J. Shen, Z. C. Zhang, M. H. Guo, K. Li, Y. B. Ou, P. Wei, L. L. Wang, Z. Q. Ji, Y. Feng, S. H. Ji, X. Chen, J. F. Jia, X. Dai, Z. Fang, S. C. Zhang, K. He, Y. Y. Wang, L. Lu, X. C. Ma, and Q. K. Xue, *Science* **340**, 167 (2013).
- [7] W. K. Tse and A. H. MacDonald, *Phys. Rev. Lett.* **105**, 057401 (2010).
- [8] X. L. Qi, R. D. Li, J. D. Zang, and S. C. Zhang, *Science* **323**, 1184 (2009).
- [9] P. Larson and W. R. L. Lambrecht, *Phys. Rev. B* **78**, 195207 (2008).
- [10] C. Niu, Y. Dai, M. Guo, W. Wei, Y. Ma, and B. Huang, *App. Phys. Lett.* **98**, 252502 (2011).
- [11] J. Henk, M. Flieger, I. V. Maznichenko, I. Mertig, A. Ernst, S. V. Eremeev, and E. V. Chulkov, *Phys. Rev. Lett.* **109**, 076801 (2012).
- [12] J. M. Zhang, W. M. Ming, Z. G. Huang, G. B. Liu, X. F. Kou, Y. B. Fan, K. L. Wang, and Y. G. Yao, *Phys. Rev. B* **88**, 235131 (2013).
- [13] Y. Li, X. Zou, J. Li, and G. Zhou, *J. Chem. Phys.* **140**, 124704 (2014).
- [14] M. G. Vergniory, M. M. Otrokov, D. Thonig, M. Hoffmann, I. V. Maznichenko, M. Geilhufe, X. Zubizarreta, S. Ostanin, A. Marmodoro, J. Henk, W. Hergert, I. Mertig, E. V. Chulkov, and A. Ernst, *Phys. Rev. B* **89**, 165202 (2014).
- [15] Y. S. Hor, P. Roushan, H. Beidenkopf, J. Seo, D. Qu, J. G. Checkelsky, L. A. Wray, D. Hsieh, Y. Xia, S.-Y. Xu, D. Qian, M. Z. Hasan, N. P. Ong, A. Yazdani, and R. J. Cava, *Phys. Rev. B* **81**, 195203 (2010).
- [16] I. Vobornik, U. Manju, J. Fujii, F. Borgatti, P. Torelli, D. Krizmancic, Y. S. Hor, R. J. Cava, and G. Panaccione, *Nano Lett.* **11**, 4079 (2011).
- [17] I. Vobornik, G. Panaccione, J. Fujii, Z. H. Zhu, F. Offi, B. R. Salles, F. Borgatti, P. Torelli, J. P. Rueff, D. Ceolin, A. Artioli, M. Unnikrishnan, G. Levy, M. Marangolo, M. Eddrief, D. Krizmancic, H. W. Ji, A. Damascelli, G. van der Laan, R. G. Egdell, and R. J. Cava, *J. Phys. Chem. C* **118**, 12333 (2014).
- [18] Q. Liu, C. X. Liu, C. K. Xu, X. L. Qi, and S. C. Zhang, *Phys. Rev. Lett.* **102**, 156603 (2009).
- [19] S. Barnes, *Adv. Phys.* **30**, 801 (1981).
- [20] M. el Kholdi, M. Averous, S. Charar, C. Fau, G. Brun, H. Ghoumaribouanani, and J. Deportes, *Phys. Rev. B* **49**, 1711 (1994).
- [21] S. Isber, S. Charar, V. Mathet, C. Fau, and M. Averous, *Phys. Rev. B* **51**, 15578 (1995).
- [22] X. Gratens, S. Isber, S. Charar, C. Fau, M. Averous, S. K. Misra, Z. Golacki, M. Ferhat, and J. C. Tedenac, *Phys. Rev. B* **55**, 8075 (1997).
- [23] H. J. von Bardeleben, J. L. Cantin, D. M. Zhang, A. Richardella, D. W. Rench, N. Samarth, and J. A. Borchers, *Phys. Rev. B* **88**, 075149 (2013).
- [24] R. S. Silva, H. D. Mikhail, R. Pavani, N. F. Cano, A. C. A. Silva, and N. O. Dantas, *J. Alloys Comp.* **648**, 778 (2015).
- [25] J. S. Dyck, P. Hájek, P. Lošťák, and C. Uher, *Phys. Rev. B* **65**, 115212 (2002).
- [26] C. W. Rischau, B. Leridon, B. Fauque, V. Metayer, and C. J. van der Beek, *Phys. Rev. B* **88**, 205207 (2013).
- [27] H. Köhler, *Physica Status Solidi B* **74**, 591 (1976).
- [28] C. M. Jaworski, V. Kulbachinskii, and J. P. Heremans, *Phys. Rev. B* **80**, 233201 (2009).
- [29] V. A. Kulbachinskii, N. Miura, H. Nakagawa, C. Drasar, and P. Lostak, *J. Phys.: Condens. Matter* **11**, 5273 (1999).
- [30] V. A. Kulbachinskii, V. G. Kytin, A. A. Kudryashov, and P. M. Tarasov, *J. Solid State Chem.* **193**, 47 (2012).
- [31] N. H. Jo, K. Lee, J. Kim, J. Jang, J. Kim, and M. H. Jung, *App. Phys. Lett.* **104**, 252413 (2014).
- [32] A. Abragam and B. Bleaney, *Electron Paramagnetic Resonance of Transition Ions* (Clarendon, Oxford, 1970).
- [33] J. H. Van Vleck, *Phys. Rev.* **74**, 1168 (1948).
- [34] P. W. Anderson and P. R. Weiss, *Rev. Mod. Phys.* **25**, 269 (1953).
- [35] E. A. Turov, *Physical Properties of Magnetically Ordered Crystals*, edited by A. Tybulewicz and S. Chomet (Academic, New York, 1965).
- [36] C. Kittel, *Phys. Rev.* **73**, 155 (1948).
- [37] The shifts of the resonance line due to the shape and magnetocrystalline anisotropy have been observed in the ferromagnetic resonance study of the thin films of $\text{Bi}_{2-x}\text{Mn}_x\text{Se}_3$ in Ref. [23].
- [38] H. Benner and J. P. Boucher, *Spin Dynamics in the Paramagnetic Regime: NMR and EPR in Two-dimensional Magnets*, in *Magnetic Properties of Layered Transition Metal Compounds*, edited by L. I. de Jongh (Kluwer, Dordrecht, 1990).
- [39] J. Korryng, *Physica* **16**, 601 (1950).
- [40] F. Matsukura, H. Ohno, A. Shen, and Y. Sugawara, *Phys. Rev. B* **57**, R2037(R) (1998).